Scanning X-ray diffraction microscopy for diamond quantum sensing

Mason C. Marshall, ^{1,2,3} David F. Phillips, ² Matthew J. Turner, ^{3,4,5} Mark J.H. Ku, ^{3,6,7} Tao Zhou, ⁸ Nazar Delegan, ^{9,10} F. Joseph Heremans, ^{9,10,11} Martin V. Holt, ⁸ and Ronald L. Walsworth ^{1,2,3,12}

¹Department of Electrical Engineering and Computer Science,
University of Maryland, College Park, Maryland, 20742, USA

²Center for Astrophysics | Harvard & Smithsonian, Cambridge, Massachusetts, 02138, USA

³Quantum Technology Center, University of Maryland, College Park, Maryland, 20742, USA

⁴Department of Physics, Harvard University, Cambridge, Massachusetts, 02138, USA

⁵Center for Brain Science, Harvard University, Cambridge, Massachusetts, 02138, USA

⁶Department of Physics and Astronomy, University of Delaware, Newark, Delaware, 19716, USA

⁷Department of Materials Science and Engineering,
University of Delaware, Newark, Delaware, 19716, USA

⁸Center for Nanoscale Materials, Argonne National Laboratory, Lemont, Illinois, 60439, USA

⁹Center for Molecular Engineering, Argonne National Laboratory, Lemont, Illinois, 60439, USA

¹⁰Materials Science Division, Argonne National Laboratory, Lemont, Illinois, 60439, USA

¹¹Pritzker School of Molecular Engineering, University of Chicago, Chicago, Illinois, 60439, 60637, USA

¹²Department of Physics, University of Maryland, College Park, Maryland, 20742, USA

(Dated: Draft: December 24, 2024)

Understanding nano- and micro-scale crystal strain in CVD diamond is crucial to the advancement of diamond quantum technologies. In particular, the presence of such strain and its characterization present a challenge to diamond-based quantum sensing and information applications – as well as for future dark matter detectors where directional information of incoming particles is encoded in crystal strain. Here, we exploit nanofocused scanning X-ray diffraction microscopy to quantitatively measure crystal deformation from growth defects in CVD diamond with high spatial and strain resolution. Combining information from multiple Bragg angles allows stereoscopic three-dimensional reconstruction of strained volumes; the diffraction results are validated via comparison to optical measurements of the strain tensor based on spin-state-dependent spectroscopy of ensembles of nitrogen vacancy (NV) centers in the diamond. Our results open a path towards directional detection of dark matter via X-ray measurement of crystal strain, and provide a new tool for diamond growth analysis and improvement of defect-based sensing.

I. INTRODUCTION

Recently, quantum defects in diamond have emerged as a popular and growing platform for a variety of sensing applications [1–5]. While defect-ensemble based sensing can achieve extremely high spatial resolution and sensitivity, these capabilities are subject to the host diamond's homogeneity and quality [6, 7]. Intrinsic strain in diamond limits many defect-based sensing applications; understanding and optimizing the defect's local crystallographic environment is therefore a major effort in the quantum sensing and diamond growth communities [6-8]. In particular, strain features with spatial structure near or below the visible-light diffraction limit are difficult to characterize via existing techniques such as optical birefringence [9] or nitrogen vacancy (NV) center spectroscopy [6, 10, 11]. However, such strain features negatively impact sensing applications by broadening quantum defect spin transition linewidths, thereby limiting their overall sensitivity to electromagnetic fields, temperature, and other phenomena [6]. Additionally, the boundaries of crystallographic strain defects act as charge traps [12], which may have deleterious effects on sensing via reduced spin coherence [13, 14]. These issues are compounded by the need for fabricated optical microstructures and nanophotonic features for quantum information processing using NV centers and other defects in diamond [15, 16], which result in large strain over submicron length scales [17]. A technique capable of characterizing short-length strain is necessary to better understand the interplay between local strain features and quantum point-defect sensors.

Strain sensing below the optical diffraction limit is also a crucial element of a proposed dark matter (DM) detector in diamond capable of sensing the direction of incident particles [18]. Diamond is a promising target material for future detectors aimed at weakly interacting massive particles (WIMPs) and similar DM candidates [19]. Lasting crystal damage from WIMP collisions would act as a memory for the direction of the incoming particle, and would be read out via a multi-step detection process outlined in Sec. V. This directional information would enable discrimination from background solar and other neutrinos expected to limit the next generation of WIMP searches [20, 21]. Demonstrating sensitive, high-spatial-resolution strain measurement in diamond is an important step towards such a detector [22].

All of the applications highlighted here could also benefit from understanding the three-dimensional topology of strain features. Currently, a variety of techniques are used to produce low strain in quantum defect-hosting diamonds, including substrate surface treatment before CVD deposition and annealing of CVD layers [7, 8]. Understanding the three-dimensional topology of remaining,

small-magnitude strain features, and their evolution under such processes, could help optimize diamond growth and thus improve sensing performance. Finally, a three-dimensional measurement would also provide a fuller understanding of the strain around and within fabricated microstructures, and allow prediction and mitigation of their effect on nearby defects.

In this paper, we demonstrate that scanning X-ray diffraction microscopy (SXDM) is a versatile technique for performing such three-dimensional, sub-micron strain measurements in diamond. Using the Hard X-ray Nanoprobe (HXN) at the Advanced Photon Source at Argonne National Laboratory [23] - illustrated schematically in Fig. 1a - we characterize the micro- and nanoscale strain environment in a diamond used for NV magnetic-field sensing, demonstrating both resolution below the visible-light diffraction limit and stereoscopic three-dimensional imaging. Lateral resolution at or below 10 nm is regularly achieved on this instrument [24–26]. Depth resolution in a bulk crystal is usually limited by the X-ray nanobeam's focal length of approximately 10 μ m. We also demonstrate a strain feature lineshape analysis technique that enables quantitative measurement of small, highly strained volumes occupying a subset of the beam length.

The NV sensing diamond used has a 40 μ m-thick, nitrogen-doped layer, with a high density of NV centers. This layer was grown by (001) chemical vapor deposition (CVD) atop an electronic-grade diamond substrate with very low nitrogen and NV content. This particular sample has large-scale strain gradients and imperfections, and is representative of the types of crystal structure found in nitrogen-doped diamonds grown for NV sensing; for more sample details, see Supplemental Material sec. VIII A. Despite the presence of a broad, inhomogeneous overall strain distribution, the strain feature lineshape analysis technique enables measurement of dislocation defects within the NV-rich CVD layer. By combining measurements taken at two different Bragg angles and using prior information about growth conditions and the likely origin of defects, we construct a threedimensional model of growth features. We validate this analysis via comparison to lower-spatial-resolution optical strain measurements performed via NV center spinstate spectroscopy, and demonstrate the complementary advantages of the two techniques. Finally, we characterize both detection sensitivity and background levels in the context of the proposed dark matter detector, demonstrating a viable path to directional DM detection.

II. SCANNING X-RAY STRAIN MEASUREMENTS IN DIAMOND

At the HXN, a bright, monochromatic beam of hard X-rays is focused to spot sizes of 10-25 nanometers by a Fresnel zone plate [24]. The sample is held at the Bragg angle for some crystallographic plane while the beam spot

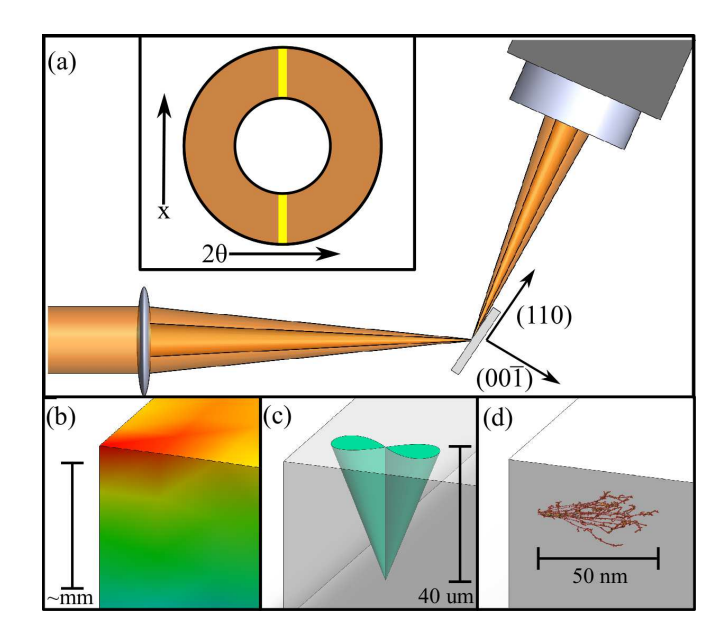


FIG. 1. (a) Illustration of scanning X-ray diffraction microscopy (SXDM). A monochromatic beam of hard X-rays (11.2 keV in the experiments reported here) is focused to a 25-nanometer spot at the sample surface. X-rays undergo Bragg diffraction from crystal planes inside the sample, and are collected by a pixelated detector. The beam position is scanned across the sample surface, and a diffraction pattern is collected at each position. Inset: Simplified schematic of the beam profile (orange ring). The narrow vertical yellow bar illustrates a simple diffraction pattern, representative of X-rays that would be imaged by the detector for a perfect bulk crystal. Strain in the crystal shifts the Bragg angle θ , moving the diffraction pattern along the detector 2θ axis. (b)-(d) Illustrations of different crystal strain features discussed in this work. (b) Macroscopic strain gradients arise across the diamond, for example due to cleavage of a diamond into segments. (c) Dislocation features incorporated during CVD growth may create regions of strained crystal. (d) Microscopic damage to the diamond crystal - such as nuclear recoils following a WIMP or neutrino impact - leave characteristic strain signatures associated with displaced carbon nuclei in the lattice.

is scanned across the sample surface [27]. At each point, a diffraction pattern is recorded on a two-dimensional photon counting pixel detector. The position, shape, and intensity of the measured diffraction pattern encode the local crystal structure sampled by the beam, including spacing and orientation of the diffracting crystal planes as well as local impurity content [28].

As the X-ray beam travels through the diamond, it interacts with several distinct volumes, schematically illustrated in Fig. 2a. The uppermost, NV-enriched overgrowth layer hosts crystal growth defects, which nucleate at imperfections on the substrate surface and exhibit large strains relative to the surrounding diamond. The surface at the substrate-layer interface was mechanically polished before CVD overgrowth, resulting in sub-surface

damage and creating a broad strain distribution [7]. Finally, the substrate is a 500 μ m-thick high-purity diamond plate.

At a particular beam position, the diffraction pattern registered on the detector combines information from all the diamond layers with which the beam interacts. As the beam is scanned in two dimensions across the diamond surface, strain features at different depths in the crystal are therefore projected at an angle determined by the Bragg condition (as illustrated in Figs. 2b and 2c). In order to reconstruct the depth structure of strain features, we use two distinct Bragg angles, giving diffraction from the crystal planes with Miller indices (113) and $(\overline{1}13)$; combining the information from two projections allows us to constrain the three-dimensional structure of strains in the sample. Additionally, SXDM is sensitive to the spacing between the diffracting crystallographic planes, and therefore measures the projection of strain along the diffracting crystal axis; comparing measurements made at different Bragg conditions allows characterization of anisotropy in a strain feature.

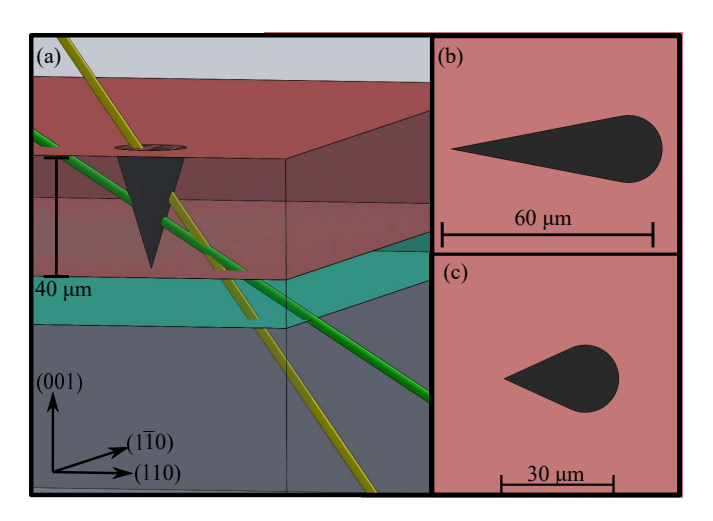


FIG. 2. (a) Schematic for hard X-ray nanoprobe (HXN) interrogation of the (113) and ($\bar{1}13$) crystal planes. The green beam addresses the (113) plane, while the yellow beam addresses ($\bar{1}13$). Layers with different lattice spacings and orientations diffract X-rays within the beam differently, creating the diffraction pattern of Fig. 3a. Schematically represented diamond components are: high-purity CVD substrate (gray), polishing damage layer at substrate surface (green), NV-doped CVD overgrowth layer (red), which contains strained growth defect features (black). Right side: Schematic of strained growth defect feature as projected onto the surface by scans addressing the (b) (113) and (c) ($\bar{1}13$) crystal planes.

The lattice spacing and crystal orientation vary through the diamond volume due to defect-induced strain, impurity content, and mechanical processing damage. The diffraction pattern combines the contributions from all of these independent, spatially varying effects. An example diffraction pattern acquired with the HXN is shown in Fig. 3a. The diffraction pattern from an ideal,

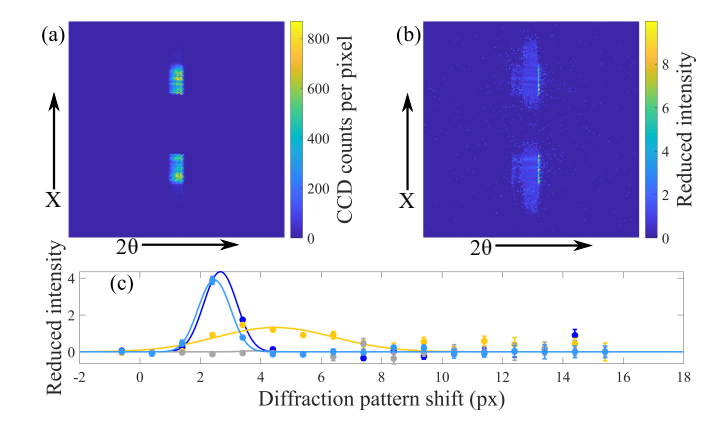


FIG. 3. (a) Diffraction pattern in a diamond sample measured at a single X-ray beam position, which includes contributions from multiple layers of the diamond as sketched in Fig. 2. (b) Diffraction pattern of (a) after dividing by the local host-crystal diffraction profile (see supplemental material Sec. B for details). This ratio emphasizes the contribution from sharp, small-length-scale strain features like crystal growth defects or recoil-induced damage. Each column of pixels in (b) is summed, yielding a 1-dimensional diffraction curve, four of which are shown in (c). Each diffraction curve is fit to a Gaussian lineshape to extract a centroid and linewidth. The centroid position gives the mean strain in the feature, while the linewidth depends on the feature's thickness along the beam path. Line colors are chosen to approximately match the strain scale of Fig. 4.

unstrained, 40 μ m-thick diamond would appear as a single column of detector pixels in Fig. 3a [29, 30]; the broad peak observed here arises from multiple complicating factors, including a variety of strain states among the layers as well as interactions at the layer interfaces.

Creating a full analytical model of the diffraction pattern from such a sample requires detailed microscopic models for vacancy and impurity incorporation during the different CVD growth steps, for polishing damage at the substrate surface, and for crystal structure and Xray diffraction behavior at the substrate-overgrowth interface. Developing such models is challenging because of the complexity of the stochastic processes involved. as well as the proprietary nature of diamond growth parameters. Instead, we develop a method to analyze local strain features in the overgrowth layer, independent of the complex but slowly spatially-varying overall lineshape of the diffraction pattern associated with the layered diamond structure. Specifically, we focus on micrometer-to-nanometer-scale volumes strained relative to the surrounding crystal - the features whose interrogation is most relevant to quantum sensor coherence properties and dark matter detection applications, and which can uniquely be addressed through SXDM. Two such features are schematically illustrated in Fig. 1: the clover-shaped dislocation feature of panel (c) and the nuclear recoil track of panel (d). Conversely, the strain gradient of panel (b) would contribute to the slowly vary-

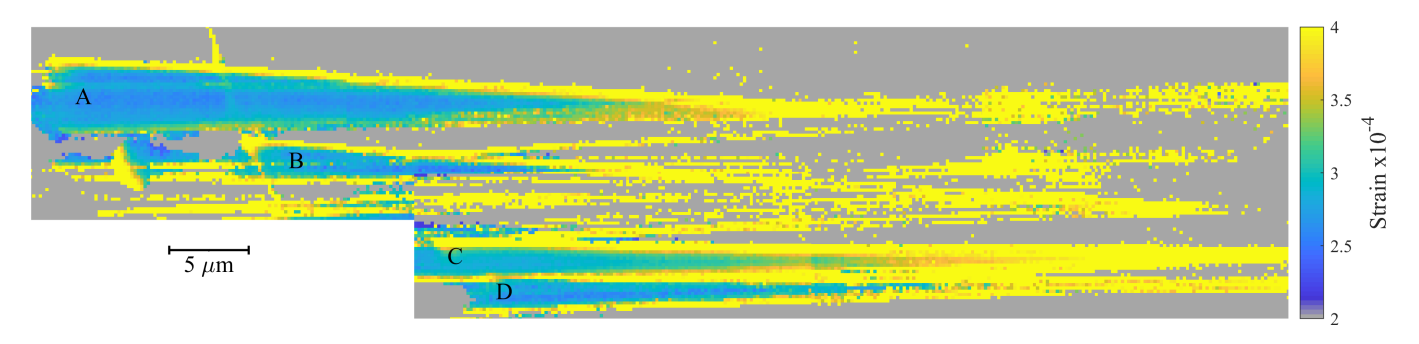


FIG. 4. Spatial map of strain due to crystal dislocation features in one region of diamond sample used in this study, as measured with (113) diffraction. Grey indicates X-ray beam positions that do not intersect a strain feature, as identified via a threshold on the amplitude of the reduced diffraction curve, as illustrated in Figure 3c. The four most prominent features are labeled A-D to simplify discussion in the main text.

ing overall lineshape of the diffraction pattern, and thus would not be highlighted in our analysis; strain over these larger length scales can be more easily measured by other methods (see Sec. IV).

To isolate and quantitatively analyze short-length strain features, we use an empirical lineshape reduction technique, illustrated in Fig. 3b-c. First, we construct a local host-crystal diffraction profile, by averaging diffraction patterns from nearby positions where the X-ray beam does not intersect strain features. (See Supplemental Material Sec. VIII C for detail on how this profile is constructed.) We then divide the measured diffraction pattern pixel-by-pixel with the host-crystal diffraction profile. This de-emphasizes the slowly varying overall lineshape and highlights the diffraction contribution from local strain features, resulting in a "reduced diffraction pattern" as shown in Fig. 3b. Crystal strain changes the Bragg angle θ . This is measured as shifts of the diffraction pattern along the detector's 2θ axis, chosen to lie in-plane with the Bragg angle. We therefore sum each column of the reduced diffraction pattern to create a diffraction curve, as shown in Fig. 3c. Finally, we fit these curves to a Gaussian lineshape and extract the centroid position. (A Gaussian is chosen because the spread of local impurity concentrations and strains within the beam spot should be approximately normally distributed). These measurements are sensitive to changes in both spacing and orientation of the diffracting crystal planes; sensitivity to both of these effects is valuable, as both types of lattice distortion affect defect-based sensing and both are expected to occur in a particle track. Comparing the results obtained from two Bragg angles and incorporating information from the two-dimensional shape of the diffraction pattern can constrain, but not completely determine, the contributions of these effects (see Supplemental Material, section VIII B). To evaluate the sensitivity of this measurement and to quantify the amount of lattice distortion observed in our sample, we analyzed the data in the case of uniform lattice orientation, where the signal arises entirely from strain-induced changes in the lattice spacing. Fig. 4

demonstrates the results of this analysis.

To convert from the centroid position of the reduced lineshape to strain under this uniform-orientation condition, we generate calibration curves calculated using kinematic diffraction theory for a multilayer diamond structure [29, 31]. Details of the generation of these curves are provided in the supplemental materials Sec. VIII D. Our sample is thick enough for dynamical diffraction effects to manifest [30, 32], but the resultant uncertainty in measured strain is small compared to other sources see Supplemental Material Sec. VIII F for details.

Fig. 4 shows a map of strain features in one region of the diamond, as projected onto the (113) crystal axis. Each X-ray beam position is categorized, based on whether the amplitude of the reduced diffraction curve is greater than a threshold, as either part of a strain feature or as only containing the host crystal. Points where the beam does not intersect a strain feature are greved out in Fig. 4; for strain feature points, the calibrated strain is plotted at each beam position. The strain magnitude is determined from the centroid of the diffraction curve fit and the calibration curves. Four extended growth defects are clearly identifiable as blue regions labeled A-D in this map, with internal strains (in the uniformly oriented case) of $2.5 - 3 \times 10^{-4}$. We note that lattice distortion in the features is high at the edges, while feature centers exhibit a smoothly varying structure. This ability to resolve differences in deformation within a growth defect demonstrates the power of SXDM and our lineshape analysis technique for investigating crystal growth and defect incorporation.

In addition to these four extended defect regions, we also measure several thin, linear high-distortion features; these are most likely the edges of extended defect regions exhibiting strain in a direction to which we are less sensitive (although some may be individual linear defects). Bragg diffraction measures changes in the spacing between crystallographic planes - in other words, the projection of strain onto the axis of diffraction. For strain within growth features in diamond, the Burgers vector - the direction of the crystal lattice distortion - generally

points along one of the $\langle 110 \rangle$ family of crystal axes [33]. Unit vectors for axes in this family can have dot products of 0.9, 0.4 or 0 with the (113) and ($\bar{1}13$) mirror planes used in our measurements. For example, if a feature has a (101) Burgers vector, a (113) diffraction measurement would yield 0.9 times its nominal strain, while a measurement with ($\bar{1}13$) diffraction would only yield 0.4 times the nominal strain. Comparing the projection onto different crystal planes thus allows us to constrain the Burgers vector within particular strain features.

The width of the diffraction peak due to the surrounding crystal and substrate, together with the lineshape reduction technique, imposes a minimum detectable strain threshold on our measurements of local strain features. The lineshape analysis allows us to quantitatively investigate strain features in the top CVD layer, despite the presence of a broad and spatially inhomogeneous strain distribution in the surrounding crystal. However, it also suppresses features whose diffraction peaks are insufficiently shifted from the host-crystal diffraction profile. To be detectable with low uncertainty, a feature must have enough strain for its diffraction peak to be shifted out of the slowly varying overall diffraction profile. The actual minimum threshold depends on the linewidth of the host-crystal diffraction peak; in this sample it is ~ 1.5 detector pixels. (See Supplemental Material Sec. VIII G for more details.) This leads to a minimum measurable compressive strain of $\sim 1.6 \times 10^{-4}$.

For features in certain projections we may only detect the high-strain edges, while the strain in their central regions would be below this threshold. For example, features A and C of Fig. 4 have the same strain projection when measured with both $(\bar{1}13)$ and (113) diffraction. Therefore, assuming a small contribution from lattice orientation changes, their Burgers vectors are likely along (011). Conversely, only the edges of features B and D are measurable using $(\bar{1}13)$ diffraction, meaning their Burgers vectors likely lie along (101) (again, in the uniform-orientation case). The "rod-like" features observed in both diffraction angles are likely of similar origin, representing the high-strain edges of dislocation features whose Burgers vectors lie along the $(0\overline{1}1)$, (110)or $(\bar{1}10)$ axes, with small projections onto both of our diffracting planes. The measured strain at the centers of features A-D in Fig. 4 is about $2.5 - 3 \times 10^{-4}$. For features B and D, which we hypothesize have (101) Burgers vectors, the projection onto the $(\overline{1}13)$ diffraction axis yields strain of about $1.1 - 1.3 \times 10^{-4}$ – below the minimum measurable strain. This result is consistent with our observations, where only the edges of features B and D are visible with $(\bar{1}13)$ diffraction.

Note that this minimum detectable value applies to compressive strain. A similar analysis applies to tensile strain, which will shift the diffraction peak towards smaller 2θ . For the particular diamond sample studied here, tensile strain shifts the strain-feature-induced diffraction peak across the detector region dominated by the slowly varying overall lineshape; the lineshape reduc-

tion technique is therefore less sensitive to small tensile strain. Tensile strain at the level of $\sim 2\times 10^{-3}$ would be needed for a feature to be detectable. In practice, we only observe compressively strained regions of growth defects in the 40- $\mu{\rm m}$ overgrowth layer in this sample. In general, the method presented here is applicable to both compressive and tensile strains, with the minimum measurable strain depending on the uniformity of the host crystal. However, a major advantage of our method is the ability to extract information even in the presence of a very inhomogeneous host crystal such as the sample used in this work.

III. THREE-DIMENSIONAL STRAIN RECONSTRUCTION

High-resolution, three-dimensional strain determination within diamond samples is essential to the dark matter detection proposal discussed in section V. Additionally, three-dimensional, high-resolution strain measurements offer new possibilities for analysis of CVD diamond growth and optical structure fabrication. By combining measurements at two diffraction angles with prior information of growth conditions in this sample and established knowledge about the structure of growth defects in CVD diamond, we generate a model allowing three-dimensional reconstruction of strain features in the scanned region of interest, as shown in Fig. 5. With additional measurements at orthogonal Bragg conditions, an assumption-free three-dimensional reconstruction should be possible using this method [34, 35]; however, constraints on experimental geometry during the current demonstration limited us to the non-orthogonal (113) and $(\bar{1}13)$ mirror planes. We constrain the model with two assumptions: first, that extended defects in CVD diamond generally nucleate at the interface with the substrate and propagate close to (but not perfectly along) the growth direction [33]; and second, that the integrated strain far from a defect must converge to zero [36]. Two features that satisfy these constraints, and have been widely observed in diamonds grown under similar conditions to our sample, are linear edge or screw dislocations [33] and "petal" or "clover"-shaped extended defects [6, 37, 38]. We therefore build our three-dimensional model from such features, constrained by the diffraction measurements.

We first identify individual features in the projected strain maps, and classify them either as "petals" or "rods". We note that some of the "rods" likely represent the high-strain edges of "petal" features whose centers have (113) or $(\bar{1}13)$ projections below the measurement threshold, as discussed in Sec. II; measurements at additional projection angles would be required to resolve this ambiguity. For each identified feature, we construct a corresponding feature in our three-dimensional model, and constrain its geometrical parameters by minimizing the difference between data and model. (See Supplemen-

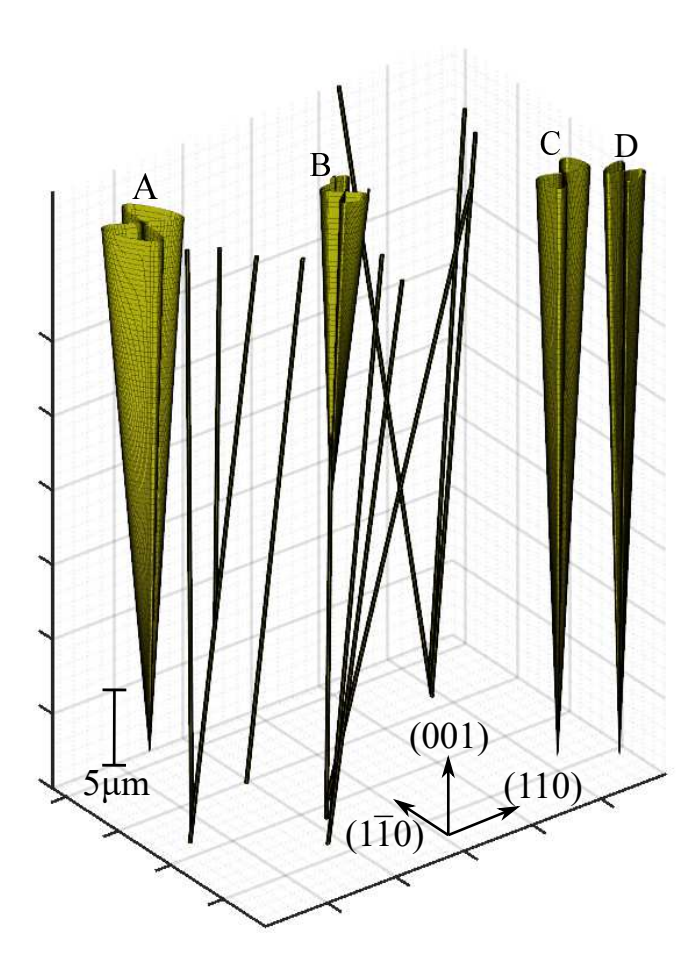


FIG. 5. Three-dimensional reconstruction of compressively strained volumes in the scanned region of the diamond sample used in this study, determined from two x-ray projections and constrained by crystal growth assumptions and an associated model of strain features (see text). Volumes indicated have strain above a threshold of 2×10^{-4} . Labeled regions correspond with labels in Fig. 4. For a schematic illustration of the projection of similar features to create data such as that presented in Fig. 4, see Fig. 16 of the Supplemental Material. For an example of the stereoscopic reconstruction of the three-dimensional model from projected data, see Fig. 17 of the Supplemental Material.

tal Material Sec. VIII I for further details on construction of the model.)

We finally note two nontrivial results obtained from this analysis. First, the strain features exhibit sharp, distinct edges where they intersect the host crystal matrix; and second, within the features we observe smoothly varying but nonuniform strain. While constructing a full microscopic model of the strained regions is beyond the scope of this work, our results to date could be taken as evidence that such clover features are constructed of sharp dislocations along the "petal" boundaries, enclosing a region of strained crystal, rather than bundles of independent linear dislocations.

IV. COMPARISON WITH STRAIN MEASUREMENTS FROM QUANTUM DIAMOND MICROSCOPE (QDM)

Optical methods for strain measurements in diamond are limited in spatial resolution by diffraction to a few hundred nm and are not in general sensitive to threedimensional spatial structure. In particular, ensemble NV spectroscopy measures integrated stress throughout the nitrogen-doped layer [6]. Despite reduced spatial and three-dimensional resolution, optical strain/stress measurements via NV spin-state spectroscopy offer complementary advantages over SXDM. Wider fields of view enable fast location of regions of interest for high-resolution diffraction measurements, which is necessary for directional WIMP detection [22]. Additionally, such optical methods are capable of measuring strain as low as 10^{-6} , albeit only as an average over an optical pixel. Finally, from a single optical measurement it is possible to reconstruct the entire strain tensor [6], which could inform the choice of Bragg angles used for diffraction.

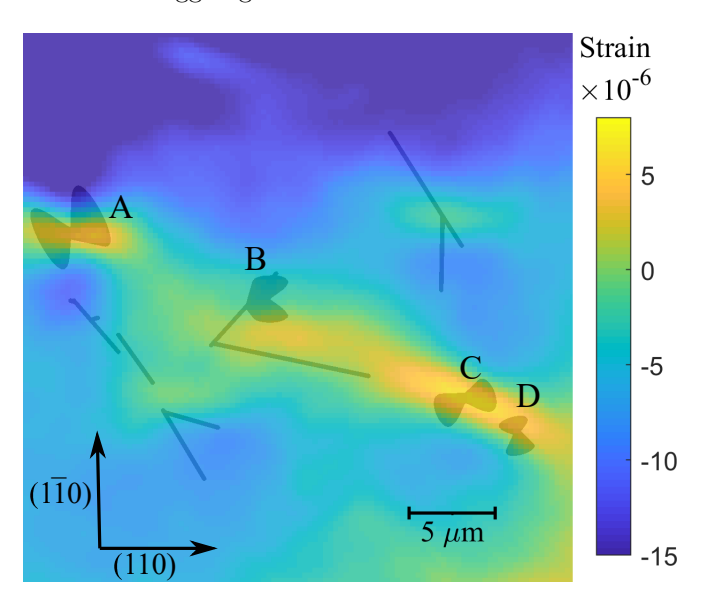


FIG. 6. Sum of strain tensor elements measured using a quantum diamond microscope (QDM), overlain with vertical projection of a three-dimensional strain reconstrution derived from SXDM measurements. Colormap and corresponding scale bar represent strain measured with QDM, while wire-frame objects are the projected reconstruction. Labeled features correspond with labels in Figs. 4 and 5.

To illustrate the complementary application of X-ray and optical methods, we used a quantum diamond microscope (QDM) [1] to image the same field of view featured in our nanoprobe diffraction measurements. In a QDM, NV centers in diamond are excited with green laser light, and their spin-state controlled with applied microwaves; the spin state and environment of the NVs can then be determined. QDMs are commonly used to image DC magnetic fields, but have also been used for sensitive

stress and strain measurements. QDM results reported in this work were performed by determining the stress Hamiltonian from NV spin-state-dependent optical measurements, using methodology and apparatus reported in [6]; the stress tensor was converted to strain using the measured elasticity tensor for diamond [39].

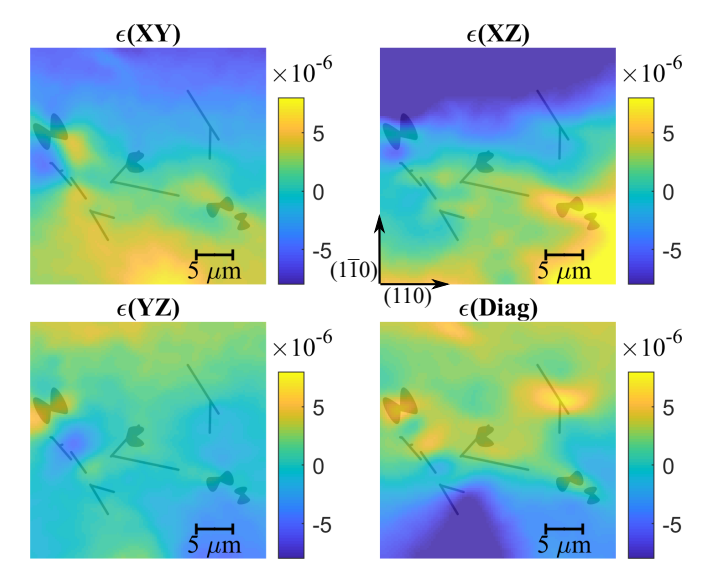


FIG. 7. Comparison between QDM strain tensor measurements and three-dimensional reconstruction of growth defect regions from SXDM measurements. Strain tensor elements $\epsilon(ij)$ give strain on the i crystal plane in the j direction; $\epsilon(\mathrm{Diag})$ is the normal strain, while the other tensor elements give shear strain. Constant offsets have been subtracted from QDM strain tensor measurements to simplify comparison on common color scales. Note the larger color scale in $\epsilon(\mathrm{XZ})$ due to an overall gradient in XZ shear strain across the region.

Figures 6 and 7 compare the three-dimensional strain reconstruction from SXDM data and our methodology with QDM strain tensor measurements. The QDM measurements demonstrate poorer spatial resolution (1-10 micron), limited by collection of light from the entire axial focal length of the microscope objective used. Nonetheless, Fig. 6 demonstrates good agreement between the two techniques with regards to strain geometry over large lengthscales. For this comparison, we sum all the strain tensor elements derived from QDM measurements to obtain a map of feature position, regardless of orientation. This serves to validate the SXDM measurement of strain features via the reduced diffraction curve, as well as the three-dimensional reconstruction. We find good agreement between the SXDM and QDM approaches for "clover" features as well as for the positions of "rod" features and strain tensor elements, supporting the hypothesis that the latter phenomena are actually the high-strain edges of features with smaller projections onto the (113) and ($\bar{1}13$) axes.

Figure 7 compares individual elements of the strain tensor from QDM measurements with the reconstructed strain features from SXDM measurements. Generically, a strain tensor element $\epsilon(ij)$ gives the change in the position of the i crystal plane along the j direction. For i=j, ϵ is the normal strain on the i planes, while for $i\neq j$ ϵ is the shear strain. The comparison in Fig. 7 shows the additional information that can be gained from performing both QDM and X-ray diffraction measurements on the same sample. The QDM illuminates the direction of shear strains and gives information about strain on longer length scales, while the nanoprobe measurement gives higher spatial resolution and reveals the three-dimensional structure of the strain features.

We note that several other methods have been applied to optically measure strain in CVD diamond, although none fills the role of SXDM for high-resolution, threedimensional strain measurements. Optical birefringence measures strain integrated through the length of the crystal [9]. Bulk X-ray tomography has been applied to similar CVD diamonds: it provides three-dimensional images, but suffers from lower spatial and strain resolution than SXDM [33]. Strain measurements using spectroscopy of single NV centers are perhaps the most comparable to SXDM in terms of obtaining three-dimensional information [11]. However, the need to resolve individual NV centers in the bulk of the diamond limits the spatial resolution to the ~micron level, and limits the technique's application to diamonds with a narrow range of NV densities.

V. TOWARDS DARK MATTER DETECTION

We finish by characterizing the performance of the SXDM strain mapping technique in the context of the proposed directional WIMP detector, see Fig. 8 [18, 22]. We can estimate the strain signal from a WIMP collision following [22], and compare to the sensitivity analysis of Sec. II. We scale the strain per crystal lattice vacancy by the number of vacancies created [18] and the r^{-3} distance scaling of strain due to point defects [36]. For a particle scattering event imparting 10 keV to a carbon nucleus — the low end of a diamond detector's directional sensitivity range [18] — the average strain within 30 nm of the resulting damage track will be $\sim 1.8 \times 10^{-4}$. This would be detectable with the SXDM technique even with the imperfect, highly inhomogeneous diamond sample used in this demonstration. In an ideal detector segment – a homogeneous crystal without a substrate layer or mechanical polishing damage – the minimum detectable nanoscale strain with the SXDM method should be significantly smaller.

Figure 9 presents results from a background SXDM scan, taken in two arbitrarily chosen regions away from strain features large enough to appear in birefringence or QDM measurements. Figure 9b includes a group of extended linear defects whose observed strain signals are approximately 100 nm wide, demonstrating spatial resolution well below the optical diffraction limit. This matches the expected length scale of WIMP-induced

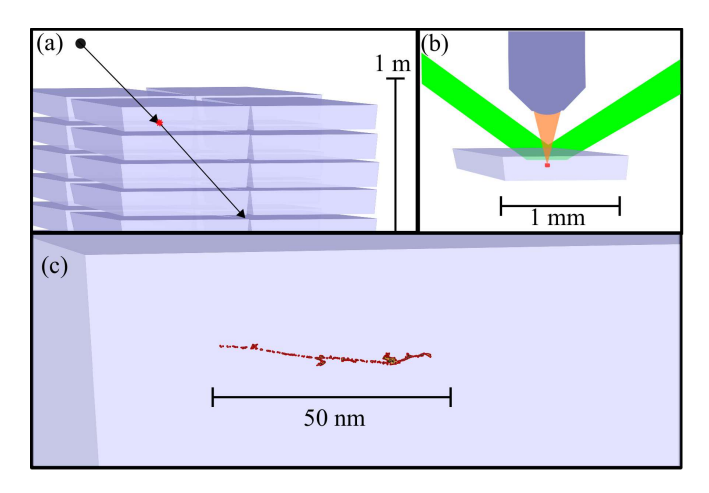


FIG. 8. Application of spatially resolved nanoscale strain measurement to dark matter detection. (a) WIMP dark matter interacts with a carbon nucleus in a sectioned diamond target, triggering detector elements. (b) Triggered section is removed from target and imaged or scanned; crystal damage due to nuclear recoils is localized to a μ m-cubed voxel. (c) Within the diamond section, the orientation and asymmetry of the damage track and resulting nanoscale strain preserve information about the incident WIMP's direction. This information can be read out using the scanning X-ray nanodiffraction techniques presented here.

damage tracks for much of the target energy range. The spatial resolution limit of the HXN is ~ 10 nm at the minimum focal size [24], which should be sufficient for resolving WIMP signatures. If required, higher resolution X-ray strain imaging is possible via advanced techniques such as Bragg projection ptychography [40, 41].

In addition to an instrument and technique capable of measuring nanoscale damage tracks in diamond, the proposed WIMP directional detection method requires production of CVD diamond crystals without pre-existing strain features that could be misidentified as damage tracks. The data in Fig. 9 represents an initial step towards demonstrating such samples; in high-resolution SXDM scans, we see no evidence of strain features with submicron extent in all three dimensions, as expected for WIMP-induced damage tracks. In Fig. 9a, despite the presence of a broad overall gradient we see no sharp features; and in Fig. 9b, we observe features that are ~ 100 nm wide but microns in length. Although further background characterization will be required before production of a directional WIMP detector, these initial results support the expectation that after high-temperature annealing, defects in CVD diamond should either be pointlike or extended, without structure at intermediate length scales ~ 100 nm in all three dimensions [7, 37].

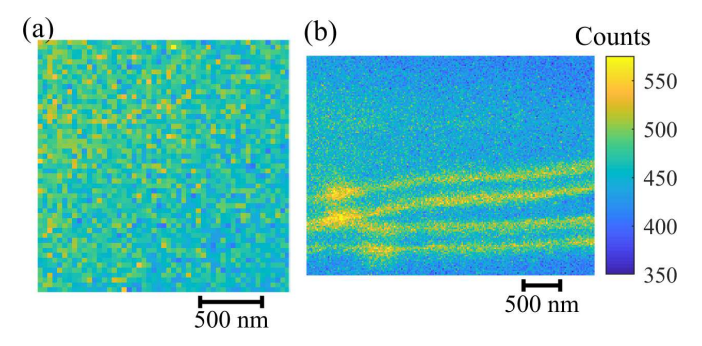


FIG. 9. SXDM scans of representative "background" regions, away from distinct strain features, demonstrate the absence of pre-existing features that could be mistaken for WIMP recoil tracks. Each plot shows the number of detector counts arising from compressively strained diamond in the CVD overgrowth layer (see supplemental material for details). (a) Despite an overall strain gradient, a 40 nm-increment scan of the nanoprobe did not find features with the ~ 100 nm length scale expected for WIMP tracks. (b) A scan of a different background region, this time with 20 nm increments, reveals extended dislocation bundles, which can be easily distinguished from WIMP recoil tracks by their length; again no strain features are observed having ≤ 100 nm scale in all three dimensions.

VI. CONCLUSION

We performed scanning X-ray diffraction microscopy (SXDM) with high spatial and strain resolution on a CVD diamond sample featuring a 40 micron layer of dense nitrogen vacancy (NV) centers. Using an empirical lineshape reduction technique applied to SXDM diffraction curves, we measured the strain in small growth defect volumes within the crystal matrix, despite a broad, inhomogeneous diffraction signal arising from the sample's layered structure and its high impurity content. Such measurements could grant valuable insight into defect development and mitigation during diamond growth, with important implications for future defect-based quantum sensing efforts, as well as for the development of diamond structure fabrication.

By combining measurements at two diffraction conditions, we created a three-dimensional strain reconstruction of the growth defects, which was found to be in good agreement with and complementary to stress measurements performed with NV spin-state spectroscopy using a quantum diamond microscope (QDM). The combination of techniques offers a new window into the three-dimensional, microscopic structure of strain features in CVD diamond.

Finally, we evaluated the performance of the SXDM techniques for a proposed directional detector of WIMP dark matter. For the diamond sample studied here, the performance approaches or exceeds benchmarks in terms of both spatial and strain resolution; a limited initial survey found no pre-existing backgrounds to impede a

dark matter search. Such a detector technology - with high target density and directional detection capability would enable WIMP searches to push sensitivity below the neutrino floor, opening a new path for future generations of WIMP detectors.

VII. ACKNOWLEDGEMENTS

We acknowledge useful discussions and feedback from Connor Hart and Reza Ebadi. This work was supported by the DOE QuANTISED program under Award No. DE-SC0019396; the Army Research Laboratory MAQP program under Contract No. W911NF-19-2-0181; the DARPA DRINQS program under Grant No. D18AC00033; and the University of Maryland Quantum Technology Center. This work was performed in part

- at the Harvard Center for Nanoscale Systems (CNS), a member of the National Nanotechnology Coordinated Infrastructure Network (NNCI), which is supported by the National Science Foundation under NSF award no. 1541959. Work at Argonne was supported by the Center for Novel Pathways to Quantum Coherence in Materials, an Energy Frontier Research Center funded by the U.S. Department of Energy, Office of Science, Basic Energy Sciences in collaboration with the U.S. Department of Energy, Office of Science, National Quantum Information Science Research Centers. The SXDM measurements were performed at the Hard X-ray Nanoprobe Beamline operated by the Center for Nanoscale Materials and the Advanced Photon Source, both Office of Science user facilities supported by the U.S. Department of Energy, Office of Science, Office of Basic Energy Sciences, under Contract No. DE-AC02-06CH11357.
- [1] E. V. Levine, M. J. Turner, P. Kehayias, C. A. Hart, N. Langellier, R. Trubko, D. R. Glenn, R. R. Fu, and R. L. Walsworth, Nanophotonics 8, 1945–1973 (2019).
- [2] R. Schirhagl, K. Chang, M. Loretz, and C. L. Degen, Annual Review of Physical Chemistry 65, 83–105 (2014).
- [3] A. Boretti, L. Rosa, J. Blackledge, and S. Castelletto, Beilstein Journal of Nanotechnology 10, 2128–2151 (2019).
- [4] J. M. Taylor, P. Cappellaro, L. Childress, L. Jiang, D. Budker, P. R. Hemmer, A. Yacoby, R. Walsworth, and M. D. Lukin, Nature Physics 4, 810–816 (2008).
- [5] G. Balasubramanian, I. Y. Chan, R. Kolesov, M. Al-Hmoud, J. Tisler, C. Shin, C. Kim, A. Wojcik, P. R. Hemmer, A. Krueger, T. Hanke, A. Leitenstorfer, R. Bratschitsch, F. Jelezko, and J. Wrachtrup, Nature 455, 648–651 (2008).
- [6] P. Kehayias, M. J. Turner, R. Trubko, J. M. Schloss, C. A. Hart, M. Wesson, D. R. Glenn, and R. L. Walsworth, Physical Review B 100, 174103 (2019).
- [7] I. Friel, S. L. Clewes, H. K. Dhillon, N. Perkins, D. J. Twitchen, and G. A. Scarsbrook, Diamond and Related Materials 18, 808–815 (2009).
- [8] A. M. Edmonds, C. A. Hart, M. J. Turner, P.-O. Colard, J. M. Schloss, K. Olsson, R. Trubko, M. L. Markham, A. Rathmill, B. Horne-Smith, and et al., Materials for Quantum Technology (2021).
- [9] L. T. M. Hoa, T. Ouisse, D. Chaussende, M. Naamoun, A. Tallaire, and J. Achard, Crystal Growth & Design 14, 5761–5766 (2014).
- [10] D. Broadway, B. Johnson, M. Barson, S. Lillie, N. Dontschuk, D. McCloskey, A. Tsai, T. Teraji, D. Simpson, A. Stacey, J. McCallum, J. Bradby, M. Doherty, L. Hollenberg, and J.-P. Tetienne, Nano Letters 19, 4543–4550 (2019).
- [11] M. E. Trusheim and D. Englund, New Journal of Physics 18, 123023 (2016).
- [12] M. Schreck, P. Ščajev, M. Träger, M. Mayr, T. Grünwald, M. Fischer, and S. Gsell, Journal of Applied Physics 127, 125102 (2020).
- [13] X.-D. Chen, L.-M. Zhou, C.-L. Zou, C.-C. Li, Y. Dong, F.-W. Sun, and G.-C. Guo, Physical Review B 92,

- 104301 (2015).
- [14] J. Choi, S. Choi, G. Kucsko, P. C. Maurer, B. J. Shields, H. Sumiya, S. Onoda, J. Isoya, E. Demler, F. Jelezko, N. Y. Yao, and M. D. Lukin, Physical Review Letters 118, 093601 (2017).
- [15] A. Sipahigil, R. E. Evans, D. D. Sukachev, M. J. Burek, J. Borregaard, M. K. Bhaskar, C. T. Nguyen, J. L. Pacheco, H. A. Atikian, C. Meuwly, R. M. Camacho, F. Jelezko, E. Bielejec, H. Park, M. Lončar, and M. D. Lukin, Science 354, 847–850 (2016).
- [16] B. J. M. Hausmann, B. J. Shields, Q. Quan, Y. Chu, N. P. de Leon, R. Evans, M. J. Burek, A. S. Zibrov, M. Markham, D. J. Twitchen, H. Park, M. D. Lukin, and M. Lončar, Nano Letters 13, 5791–5796 (2013).
- [17] S. Knauer, J. P. Hadden, and J. G. Rarity, npj Quantum Information 6, 1–6 (2020).
- [18] S. Rajendran, N. Zobrist, A. O. Sushkov, R. Walsworth, and M. Lukin, Physical Review D 96, 035009 (2017).
- [19] N. Kurinsky, T. C. Yu, Y. Hochberg, and B. Cabrera, Physical Review D 99, 123005 (2019).
- [20] C. A. O'Hare, A. M. Green, J. Billard, E. Figueroa-Feliciano, and L. E. Strigari, Physical Review D 92, 063518 (2015).
- [21] C. Bøehm, D. G. Cerdeño, P. A. N. Machado, A. O.-D. Campo, and E. Reid, Journal of Cosmology and Astroparticle Physics 2019, 043–043 (2019).
- [22] M. C. Marshall, M. J. Turner, M. J.-H. Ku, D. F. Phillips, and R. L. Walsworth, Quantum Science and Technology (2021).
- [23] R. Winarski, M. Holt, V. Rose, P. Fuesz, D. Carbaugh, C. Benson, D. Shu, D. Kline, G. Stephenson, I. Mc-Nulty, and J. Maser, Journal of Synchrotron Radiation 19, 1056–1060 (2012).
- [24] I. Mohacsi, I. Vartiainen, B. Rösner, M. Guizar-Sicairos, V. A. Guzenko, I. McNulty, R. Winarski, M. V. Holt, and C. David, Scientific Reports 7, 43624 (2017).
- [25] S. O. Hruszkewycz, M. J. Highland, M. V. Holt, D. Kim, C. M. Folkman, C. Thompson, A. Tripathi, G. B. Stephenson, S. Hong, and P. H. Fuoss, Physical Review Letters 110, 177601 (2013).

- [26] S. O. Hruszkewycz, M. V. Holt, J. Maser, C. E. Murray, M. J. Highland, C. M. Folkman, and P. H. Fuoss, Philosophical transactions. Series A, Mathematical, physical, and engineering sciences 372, (2014).
- [27] M. Holt, R. Harder, R. Winarski, and V. Rose, Annual Review of Materials Research 43, 183–211 (2013).
- [28] B. E. Warren, X-ray Diffraction (Courier Corporation, ADDRESS, 1990), google-Books-ID: wfLBhAbEYAsC.
- [29] A. Ying, B. Osting, I. C. Noyan, C. E. Murray, M. Holt, and J. Maser, Journal of Applied Crystallography 43, 587–595 (2010).
- [30] A. Pateras, J. Park, Y. Ahn, J. A. Tilka, M. V. Holt, H. Kim, L. J. Mawst, and P. G. Evans, Physical Review B 97, 235414 (2018).
- [31] J. A. Tilka, J. Park, Y. Ahn, A. Pateras, K. C. Sampson, D. E. Savage, J. R. Prance, C. B. Simmons, S. N. Coppersmith, M. A. Eriksson, M. G. Lagally, M. V. Holt, and P. G. Evans, Journal of Applied Physics 120, 015304 (2016).
- [32] B. W. Batterman and H. Cole, Reviews of Modern Physics 36, 681–717 (1964).
- [33] M. P. Gaukroger, P. M. Martineau, M. J. Crowder, I. Friel, S. D. Williams, and D. J. Twitchen, Diamond and Related Materials 17, 262–269 (2008).
- [34] F. Hofmann, E. Tarleton, R. J. Harder, N. W. Phillips, P.-W. Ma, J. N. Clark, I. K. Robinson, B. Abbey, W. Liu, and C. E. Beck, Scientific Reports 7, 45993 (2017).
- [35] F. Hofmann, N. W. Phillips, S. Das, P. Karamched, G. M. Hughes, J. O. Douglas, W. Cha, and W. Liu, Physical Review Materials 4, 013801 (2020).
- [36] J. D. Eshelby, Journal of Applied Physics 25, 255–261 (1954).
- [37] H. Pinto, R. Jones, J. P. Goss, and P. R. Briddon, Journal of Physics: Conference Series 281, 012023 (2011).
- [38] A. Crisci, F. Baillet, M. Mermoux, G. Bogdan, M. Nesládek, and K. Haenen, physica status solidi (a) 208, 2038–2044 (2011).
- [39] C. A. Klein and G. F. Cardinale, in *Diamond Optics V* (International Society for Optics and Photonics, AD-DRESS, 1992), Vol. 1759, p. 178–193.
- [40] S. O. Hruszkewycz, M. Allain, M. V. Holt, C. E. Murray, J. R. Holt, P. H. Fuoss, and V. Chamard, Nature Materials 16, 244–251 (2017).
- [41] M. Hill, I. Calvo-Almazan, M. Allain, M. Holt, A. Ulvestad, J. Treu, G. Koblmüller, C. Huang, X. Huang, H. Yan, E. Nazaretski, Y. Chu, G. Stephenson, V. Chamard, L. Lauhon, and S. Hruszkewycz, Nano Letters 18, 811–819 (2018).
- [42] M. J. Turner, N. Langellier, R. Bainbridge, D. Walters, S. Meesala, T. M. Babinec, P. Kehayias, A. Yacoby, E. Hu, M. Lončar, R. L. Walsworth, and E. V. Levine, Physical Review Applied 14, 014097 (2020).
- [43] K. Gardner, E. Mueller, J. Tilka, and P. Evans, X-Ray Nanobeam Dynamical Diffraction Simulator, https://xray.engr.wisc.edu/nanobeamsimulation/dynamicalhtml/index.php, accessed: 2020-09-09.

VIII. SUPPLEMENTAL MATERIAL

A. Sample information

The diamond sample used in this study was produced by Element Six, inc. It features a 40 $\mu \rm m$ thick overgrowth layer, grown via (001) chemical vapor deposition atop an electronic-grade, single-crystal substrate, with less than 5 ppb of both N and NV. Before growth, the substrate was mechanically polished. The overgrowth layer was grown with isotopically purified carbon, with 99.95% $^{12}\rm C$, and doped with 10 ppm of $^{15}\rm N$. After growth, the diamond was electron-irradiated and annealed to form NV centers in the N-doped layer. The resulting NV $^-$ density is approximately 1 ppm, similar to sister samples used in previous work [6, 42].

B. Constraining contributions from changes in lattice orientation

In this work, crystal lattice strain is measured via shifts in the X-ray Bragg diffraction pattern. Similar shifts in the diffraction pattern may also result from changes of orientation in the crystal lattice. However, while straininduced changes in lattice spacing of the diffracting crystal planes can only shift the diffraction pattern along the detector 2θ axis, a changing lattice orientation can shift the diffraction pattern along either detector axis. Characterizing the position of the diffraction pattern along the detector X axis can thus help constrain the contribution of lattice orientation changes to the observed diffraction pattern shifts. We characterize such shifts by finding the edges of the central low-count region induced by the beam stop [27], shown in Fig. 10a. We find that the average vertical positions in the strain features and the overall diffraction profile are equal, as shown in Fig. 10b. This disfavors changes in lattice orientation as the main source of the observed diffraction pattern shifts, except for orientations that coincidentally yield little or no X position shift.

Comparison of the measurements performed using (113) and $(\overline{1}13)$ diffraction enable us to further constrain possible contributions from changes in lattice orientation. Features A and C of Fig. 4 exhibit a centroid shift in the reduced diffraction curve lineshape by an amount consistent with equal strain along both projections. We also observe vertical diffraction pattern shifts of one pixel or less in both projections. This constrains the possible directions of lattice orientation in these strain features to only those that yield nearly zero vertical diffraction shift for both Bragg conditions, as well as a horizontal shift consistent with equal strain. While such orientation changes cannot be ruled out by our measurements, strain with Burgers vector in the $\langle 110 \rangle$ family of crystal axes is a more plausible explanation, since it both explains the observations and is known to be a dominant class of growth defects in diamond [33]. This contributes to our choice

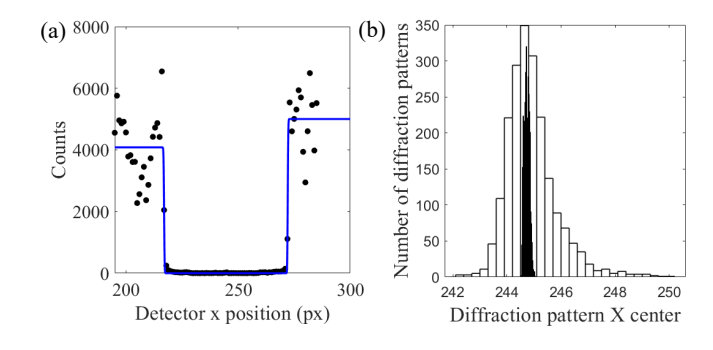


FIG. 10. (a) Representative diffraction pattern summed over the 2θ axis, together with a fit to an error function used to determine the center of the diffraction pattern along the X axis. (b) Histograms of such "X centers" for the overall diffraction pattern (black bars) and reduced diffraction pattern (white bars), for X-ray beam positions intersecting growth defect feature A (as labeled in Fig. 4). The white histogram is broader because of the comparatively fewer photons contributing to the reduced lineshape. The equal centers of these distributions favor compressive strain as the likely origin of the diffraction pattern shifts, as discussed in the text.

in section II to present results in the uniform-orientation scenario. More generally, while some of the shifts in the diffraction pattern may be caused by orientation changes as well as strain, in this work we demonstrate a sensitivity to strain sufficient, e.g., to detect WIMP dark matter signals.

C. Constructing local host-crystal diffraction profiles

In order to calculate the reduced diffraction pattern used for analysis of short-length strain features, we first construct local host-crystal diffraction profiles. This requires an initial classification of each X-ray beam position as "strained" or "host crystal" depending on whether the beam intersects a strain feature. We base this initial classification on a "region of interest" (ROI) analysis, where we define detector regions that count photons scattered by compressively strained regions of the diamond. Figure 11a shows such an ROI on an example diffraction pattern, while Fig. 11b shows a map of total counts in this ROI for all beam positions in one spatial scan. Beam positions with more than a threshold number of counts in this ROI are identified as "strained", while positions with less than this threshold are identified as interacting only with the host crystal. To determine the appropriate threshold, we measure the distribution of counts in a region of "pristine" diamond without strain features; the threshold is chosen to be approximately two standard deviations of this distribution above the mode of count numbers in each column of a spatial scan, to account for spatial intensity gradients such as that visible in Fig. 11b. We check this thresholding procedure by manually defin-

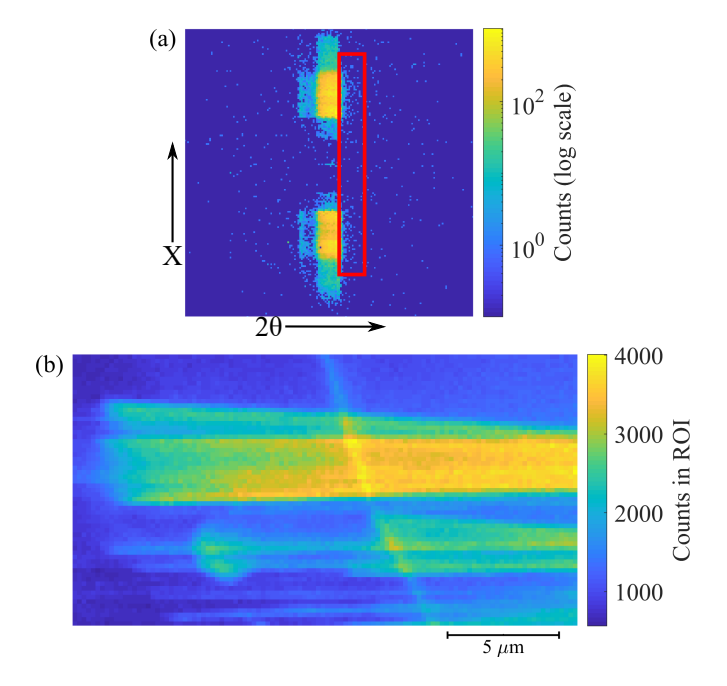


FIG. 11. (a) Example region of interest (ROI) for initial analysis to classify X-ray beam positions as "strained" or "host crystal;" the detector ROI for identifying local strain features is marked by the red box. (b) Total counts in the detector ROI for each beam position within a spatial scan.

ing "strain" and "host crystal" regions for several spatial scans; the results show good agreement. We note that this initial classification is used only to generate the host-crystal profile; in the final analysis, each beam position is re-classified based on parameters of the reduced diffraction pattern fit. The overall analysis procedure is therefore robust to occasional initial misclassifications of specific beam positions.

As can be seen in Fig. 11b, this ROI analysis reveals a smooth horizontal gradient in intensity across the field of view, likely originating from variation in the separation between sample and focusing optics as the X-ray beam is rastered across the sample. We therefore construct a separate local host-crystal diffraction profile for each column of a spatial scan by averaging all diffraction patterns from "unstrained" beam positions within that column. Dividing by the local host-crystal diffraction profile thus suppresses the inhomogeneous signal from the unstrained diamond, while simultaneously removing the effect of these horizontal gradients. This procedure yields reduced diffraction patterns such as the one featured in Fig. 3b of the main text.

D. Calibration curves

To convert between the position of the diffraction peak on the detector and the strain in the short-length-scale crystal feature, we use a calibration curve. To generate this curve, we use the kinematic approximation for crystal diffraction [29, 31] to simulate diffraction patterns for an unstrained diamond substrate with and without an additional thin strained layer, representing the strain feature. The results of one such simulation are presented in Fig. 12a. We then take the ratio between the two diffraction curves, replicating the process by which we generate the reduced diffraction patterns (as discussed in Sec. II of the main text). This gives a simulated reduced diffraction curve which can be fit to extract its centroid, as shown in Fig. 12b. Finally, this process is repeated for different strain values in the layer, generating a calibration curve, as shown in Fig. 12c.

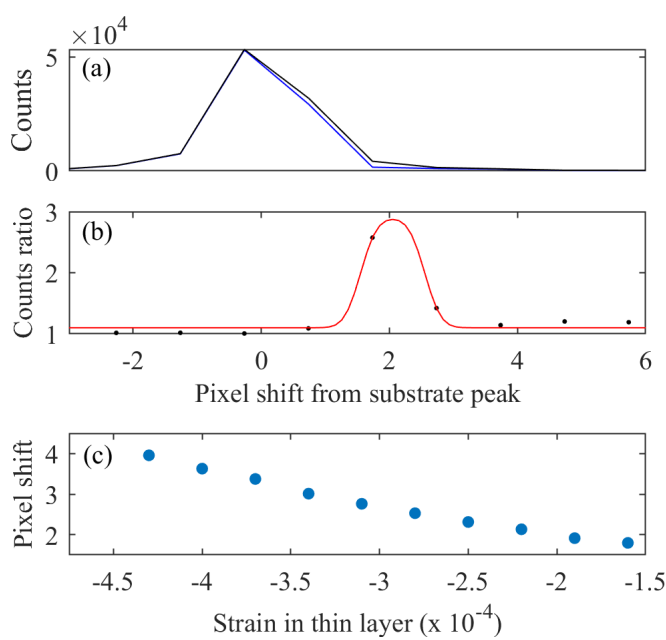


FIG. 12. Steps for generation of calibration curves to allow conversion between the X-ray diffraction peak position and and short-length-scale strain feature. (a) A diffraction curve is simulated for an unstrained substrate with (black) and without (blue) a thin layer of strained crystal. (b) Dividing these two curves gives a simulated reduced diffraction curve; this is fit to obtain its centroid. (c) This is repeated for different strain values to obtain a calibration curve.

Each point in Fig. 12a-b represents a column of detector pixels. In the real detector, these pixels count diffracted X-ray photons integrated over a finite area rather than a single point. To replicate this in our calibration and avoid possible aliasing effects, we initially oversample the simulated diffraction curve by a factor of 12; we then sum the oversampled calibration curves into bins representing the physical detector pixels.

In order to test the robustness of this calibration and characterize its uncertainty, we generated calibration curves while varying several parameters in the kinematic diffraction simulation. These include the thickness of the strained layer; the linewidth of the diffraction peak due to the unstrained substrate; the amplitude of diffraction peaks from the substrate and strained layer; the amount of oversampling performed; and the position of bin edges when summing the oversampled points. Amplitude and oversampling parameters are found not to significantly affect the calibration; uncertainty in the calibration due to strain feature thickness and unstrained diffraction peak linewidth are discussed in Supplemental Material Sec. VIII F.

E. Identifying strain feature edges via vertical asymmetry

One additional limitation of the lineshape analysis and calibration procedure relates to strain feature thickness: at positions where the X-ray beam intersects the strained feature for less than $\sim\!200$ nm, the calibration is less reliable. The Bragg diffraction peak width from a layer increases as the layer thickness decreases; for very thin layers, some portion of the diffraction peak may overlap with the large, slowly varying diffraction profile and be suppressed by the empirical lineshape reduction.

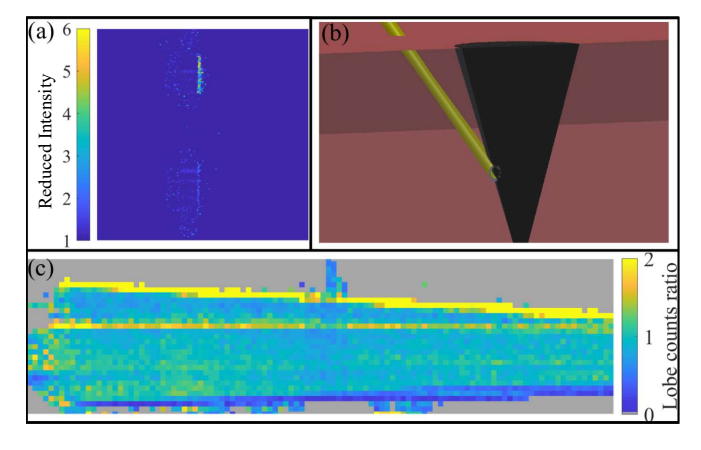


FIG. 13. Identifying region edges and narrow features using X-ray diffraction-pattern asymmetry. (a) Reduced lineshape analysis as described in section II, performed on a beam position at the edge of a strained volume. X-rays are diffracted into the feature peak for only half of the annular beam. (b) Schematic model of X-ray interactions at edge. Away from the focal plane, the beam spot size grows; at the sharp edge of a feature, only one-half of the annulus intersects the feature and diffracts X-rays to the detector. (c) Map of the top-bottom asymmetry of feature peaks, for one growth feature in the (113) projection. High or low asymmetry values signal the beam is at the edge of a feature.

To avoid miscalibrated measurements, we identify the edges of growth defects, where the intersection with the beam may be problematically short. We perform this identification by examining the two-dimensional shape of the reduced diffraction pattern. The diffraction pattern is divided into two "lobes", separated by a low-count region created by the central beam stop of the focusing optic [27] (as is visible in Fig. 3a-b of the main text).

At the atomically-sharp edges of a growth defect, these lobes will have substantially different intersections with the strain feature; away from the sharp edges, the separation between lobes is miniscule compared to the length scale of strain features. Therefore, diffraction patterns from the sharp edges of strain features show asymmetry between the two lobes, which is emphasized in the reduced diffraction pattern. Figure 13a shows a reduced diffraction pattern for such an edge, with the upper lobe having significantly more intensity after the lineshape reduction, indicating more diffraction due to the growth defect. Figure 13b shows a schematic example of a beam spot at the edge of a growth defect, with only one half of the beam intersecting the strained diamond, creating such a pattern.

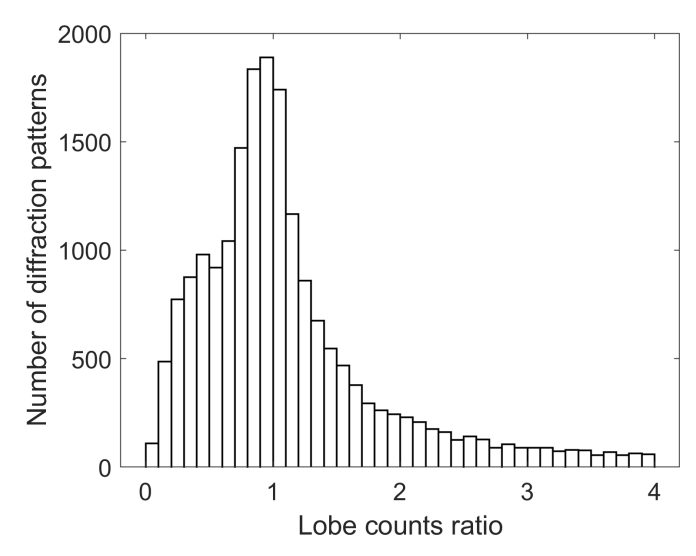


FIG. 14. Histogram of counts ratios for all X-ray beam positions featured in Fig. 4 of the main text. We label all features with count ratio less than 0.5 or greater than 2 as "edge" points.

To quantify this asymmetry, we extract the ratio of counts in the upper and lower lobes for each reduced diffraction pattern. Fig. 14 shows the distribution of this ratio for beam positions in the region of Fig. 4 of the main text. If this ratio is less than 0.5 or greater than 2, we classify that beam position as an "edge", with additional uncertainty in the calibration between diffraction curve centroid and strain due to the short distance of interaction between the beam and the strained layer. When the layer is thicker than ~ 200 nm, this calibration uncertainty is limited to 1.5E-5, as presented in table I.

F. Uncertainty in strain measurements

Section II of the main text describes the process of extracting quantitative strain values from SXDM diffraction patterns recorded on the detector. The most significant systematic uncertainties enter through the calibra-

tion curves. Table I presents the leading uncertainties for a typical measurement of a strain feature.

TABLE I. Error budget for a typical SXDM strain feature measurement using methods described in this study.

Error Source	Uncertainty
Statistical	2.0E-5
Feature thickness	1.5E-5
Unstrained peak linewidth	1.2E-5
Dynamical diffraction effects	0.9E-5
Total	2.9E-5

The thinner a strain feature is, the wider that feature's diffraction peak. Whatever part of the diffraction peak overlaps the large host-crystal diffraction peak will be suppressed when we divide to emphasize sharply varying features; the wider the true diffraction peak is, the more this suppression will shift the centroid of the reduced peak. The calibration curve therefore shows some dependence on the thickness of the strained layer, especially for very thin strain features. However, as discussed in Sec. VIII E, beam positions that only briefly interact with the edges of strain features can be distinguished by the two-dimensional distribution of counts on the detector. After removing such positions from our analysis, the remaining effect of feature thickness on the strain calibration is reflected in our error budget above.

Similarly, the linewidth of the unstrained diffraction pattern enters into the denominator of the empirical lineshape reduction analysis. The error budget reflects the range of host-crystal peak widths measured in this work.

Finally, our calibration curves are constructed using the kinematic approximation for diffraction pattern construction, while a more complete analysis would include dynamical diffraction effects. To evaluate the potential distortion due to this approximation, we benchmark our kinematic approximation calculations by comparison to publicly available dynamical diffraction code [30, 43] for the (004) mirror plane, and include the maximum observed difference as a conservative estimate of the resulting uncertainty.

G. Diffraction curves without the lineshape reduction analysis

Figure 15 shows a log-scale plot of diffraction curves before the empirical lineshape reduction analysis for the same four beam positions presented in Fig. 3c, together with the corresponding local host-crystal diffraction profiles. The ratio of measured diffraction curve to local host-crystal profile gives the reduced diffraction curves of Fig. 3c. The minimum detectable strain shift of ~ 1.5 detector pixels originates from the linewidth of the host-crystal diffraction profile; diffraction signals from features with less than this strain are suppressed in the generation of reduced diffraction curves.

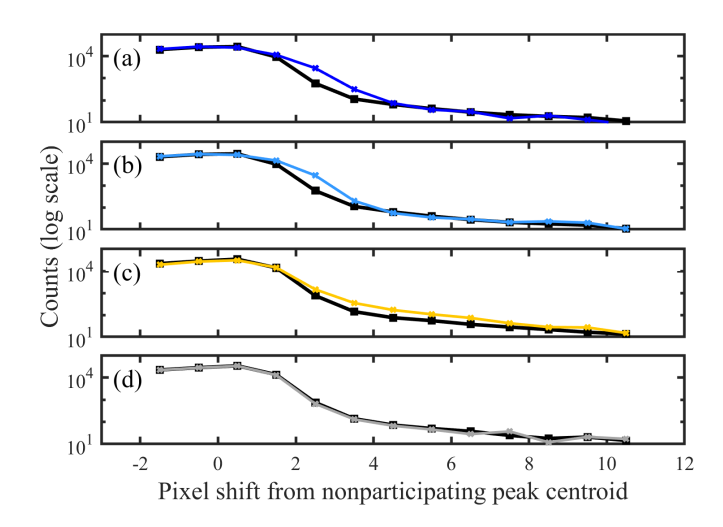


FIG. 15. Log-scale plot of SXDM diffraction curves without the empirical lineshape analysis (for the same beam positions featured in Fig. 3 of the main text and with the same colors), together with the corresponding local host-crystal diffraction profiles (black points).

H. Illustration of three-dimensional "clover" feature projected onto two-dimensional data

As discussed in the main text, the largest strain structures observed in this study take the form of "clover"-shaped growth defect regions, which nucleate at the substrate-CVD interface and propagate upwards. Only two "petals" of each clover are observed here, as opposed to the four petals in similar features observed in [6], because of the different detection thresholds for compressive and tensile strain discussed in Sec. II of the main text. Fig. 16 shows a schematic illustration of two-dimensional projection of such features by the X-ray beam, which creates (for example) the data patterns of Fig. 4.

I. Constraining geometrical parameters of the three-dimensional model

The model and procedure used in three-dimensional strain reconstruction is described in the main text. Fig. 17 gives an example of the optimization of geometric parameters of the model. The particular strain feature in this example is identified as a "petal" dislocation feature; a corresponding representation is created in the three-dimensional model. This entity is projected onto surfaces at angles corresponding to the (113) and ($\bar{1}13$) Bragg diffraction conditions. Fig. 17a-b show the data after classifying each point as either only intersecting the host crystal, part of the strained subvolume, or an edge of the strained subvolume. These classifications are made based on the amplitude of the reduced diffraction curve (see Fig. 3 of the main text) and the vertical asymmetry in the diffraction pattern (see Supplemental

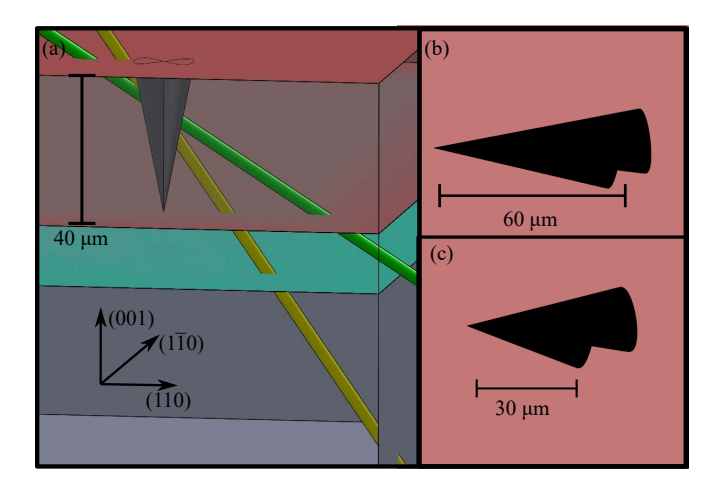


FIG. 16. Schematic of diamond interrogation with HXN. This figure demonstrates the interrogation of a two-leaf "clover" feature similar to those observed in this study. As in Fig. 2 of the main text, the green beam addresses the (113) crystal plane, while the yellow beam addresses ($\bar{1}13$). Panel (b) shows the two-dimensional projection observed by the (113) beam, while (c) shows the ($\bar{1}13$) projection.

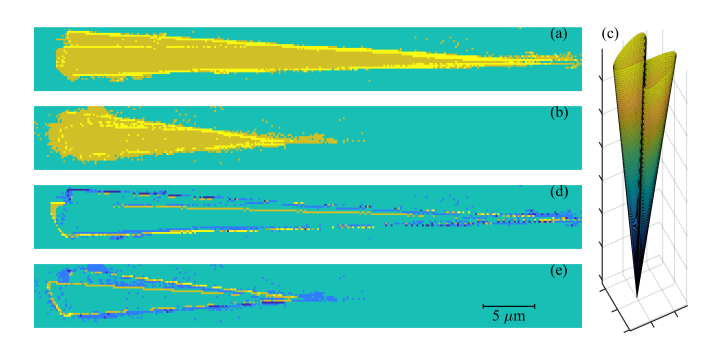


FIG. 17. Constraining 3-D strain reconstruction model parameters with SXDM data. (a)-(b): Classified data for the upper conical strain feature from the (113) (upper) and ($\bar{1}13$) (lower) projections. Each beam position is classified based on feature peak fits as only host crystal (teal), strained subvolume (orange), or edge (yellow). (c): A three-dimensional model is constructed, which can be projected onto the two measurement planes. (d)-(e): Residuals after subtracting each data set from the appropriate model projection. The sum of squared differences can be fed into a minimizing algorithm to optimize geometric parameters of the model.

Material Sec. VIIIE). Fig. 17c shows the initial threedimensional model for a "clover" feature. (Only two of the four "petals" of the "clover" are present because we only observe the compressively strained parts of the feature, while the diffraction signal from the tensile-strained "petals" is concealed by the large host-crystal diffraction profile from the substrate - see Sec. II of the main text for details.) Fig. 17d-e show the comparison between SXDM strain data and the reconstruction. To calculate residuals, we assign a value of 2 to each pixel classified as an "edge" and one to each classified as part of the strained subvolume; we subtract pixel-by-pixel to obtain the difference maps in Fig. 17d-e. To obtain a quantity that can be minimized, we sum the absolute value of all pixels in the difference maps. Minimizing these residuals gives the position, shape, size, and angle of the feature for the three-dimensional strain feature reconstruction of Fig. 5 of the main text.